APPLIED GEOPHYSICS, Vol.19, No.4 (December 2022), P. 485–502, 16 Figures.
DOI:10.1007/s11770-022-0949-z

Acoustic-electrical properties and rock physics models for shale-oil formations: prediction of reservoir properties of interbedded sandstone and shale layers

Pang Meng-Qiang[1,2], Ba Jing[1]*, Wu Chun-Fang[3], Carcione José Maria[1,4], and Müller Tobias[1]

Abstract: In recent years, the Yanchang shale-oil formations of the Ordos Basin are rich in reserves with complex lithology and structure characteristics, low porosity and low permeability, and weak anomalies for oil and water discriminations, have been the key targets of unconventional oil/gas resource exploration and development in the relevant areas. The joint acoustic-electrical (AE) properties can be used to interpret reservoir lithology, mineralogy, pore structure, and fluid saturation. To conduct tests of thin section analysis, X-ray diffraction, and ultrasonic and electrical experiments at different pressures and saturation degrees, cores from the shale-oil formations in the Q area of the basin are collected. The variations in AE properties with respect to clay content, porosity, pressure (microfracture), and saturation are analyzed. The experimental results indicate that the rock physics behaviors of sandstones with different clay contents vary significantly. The AE properties of clean sandstones are basically dependent on the microfractures (pressure), while for muddy sandstones, the clay content is an important factor affecting the responses. The target reservoir consists of interbedded sandstone and shale layers. The AE equivalent medium equations and the Gurevich theory are applied to establish the joint models for the different lithologies and simulate the variations in AE properties with respect to fluid type, pore structure, and mineral components. The three-dimensional joint templates of clean and muddy sandstones, as well as shale, are developed based on the elastic and electrical attributes and then calibrated using the experimental and well-log data. The reservoir properties are estimated with the templates and validated by the log data. The results indicate that the joint templates based on lithology characteristics can effectively characterize the properties of interbedded sandstone and shale layers. Furthermore, the combined application of AE data provides more beneficial information for the assessment of rock properties, leading to precise estimates that conform with the actual formation conditions..

Keywords: shale-oil formations, acoustic-electrical (AE) properties, interbedded layers, clay content, pore structure, rock physics model.

Introduction

With the depletion of conventional oil/gas resources and the development of petroleum industries, shale oil and tight oil reservoirs, which are widely distributed worldwide, have become extremely important targets for unconventional resource explorations (Zou et al., 2013;

Manuscript received by the Editor August 5, 2022; revised manuscript received September 7, 2022.
1. School of Earth Science and Engineering, Hohai University, Nanjingu, 211000, China.
2. Bochum University of Applied Sciences, D-44801 Bochum, Germany.
3. Shanghai Technical Institute of Electronics and Information, Shanghai, 201411, China.
4. National Institute of Oceanography and Applied Geophysics (OGS), Sgonico, Trieste 34010.
*Corresponding author: Ba Jing (Email: jba@hhu.edu.cn).

Liu et al., 2021; Shi et al., 2022). In recent years, China has shown great potential in the development of shale-oil resources. Key breakthroughs have been made in the production of shale-oil resources in the Bohai Bay Basin, Songliao Basin, Junger Basin, and Ordos Basin (Wang et al., 2020; Fan et al., 2021). The shale oil of the Ordos Basin is found to have geological reserves of tens of billions of tons, along with abundant hydrocarbon reserves (Yang et al., 2016, 2019; Liu et al., 2021). The reservoir lithology characteristics are complex, with low porosity and thin interbedded layers of sandstone, shale, and mudstone containing fine mineral grains, and the complex pore structures lead to a strong heterogeneity (Feng et al., 2013; Fan et al., 2021).

Theoretical and experimental studies have highlighted that the heterogeneity of rock microstructure may result in complex petrophysical behaviors (Amalokwu et al., 2014; Chapman et al., 2016; Ba et al., 2017; Solazzi et al., 2019; Dutilleul et al., 2020; Iwamori et al., 2021; Zhang et al., 2021, 2022). Yan et al. (2019) conducted nuclear magnetic resonance tests at different saturation states and evaluated the porosity, permeability, pore structure, and wettability of rocks using the percolation method. Sun et al. (2019) used computed tomography (CT) for the construction of three-dimensional (3D) digital cores and developed a pore network model for analyzing the effects of microfracture scale, length, and dip angle on the seepage properties. Ma and Ba (2020) calculated the intrinsic attenuation and scattering using the single isotropic scattering model and the spectral ratio method, respectively, to evaluate the effects of fluids, pore structure, and mineralogy on attenuation.

Previous studies have indicated that the rock microstructure and fluid saturation significantly affect the electrical properties (Ziarani and Aguilera, 2012; Li et al., 2015; Soleymanzadeh et al., 2021; Wang et al., 2022). Yan et al. (2017) conducted CT and X-ray diffraction (XRD) tests to simulate the fluid distribution based on the pore morphology using digital rock technology. They evaluated the effects of porosity, clay content and type, temperature, water mineralization, heavy minerals, and wettability on the oil formations with low resistivity on the basis of the sensitivity analysis. Li et al. (2020) built a 3D digital core with multiple mineral fractions and analyzed the effects of fluid saturation on electrical properties using the finite element simulation method and laboratory experiment tests.

The complex lithology, pore structure, and fluid properties of shale-oil formations lead to challenges and risks in reservoir detection methods based on a single data type. Previous studies have shown that the joint model based on the acoustic-electrical (AE) properties can help reduce the uncertainties involved in the characterizations of subsurface reservoir rocks (Kazatchenko et al., 2004; Gabàs et al., 2016; Pang et al., 2021b), which are increasingly common to investigate the rock characteristics (Gomez et al., 2010; Gabàs et al., 2016; Han et al., 2011, 2022; Pang et al., 2022). Pride et al. (2017) developed an analytical model for describing the effects of stress and fluid pressure on the elastic moduli, electrical conductivity, and permeability of rocks. Han (2018) investigated the effects of microfracture characteristics (content, density, and aspect ratio) on the AE properties based on experimental methods and theoretical models. Cilli and Chapman (2021) developed an electrical differential effective medium (DEM) theory and combined it with the elastic model to estimate the joint properties of sandstones.

The core samples of shale-oil formations in the Q area of Ordos Basin are collected to analyze the pore structure, mineralogy, and AE properties based on the XRD, cast thin sections (CTS), and ultrasonic and conductivity tests at the different pressures and saturation states. For the characteristics of sandstone-shale interbedded layers in shale-oil reservoirs, the AE Hashin–Shtrikman (HS) boundary (Mavko et al., 2009), DEM (Berryman, 1992; Cilli and Chapman, 2021), Gurevich squirt flow theory (Gurevich et al., 2010), and Gassmann equation (Gassmann, 1951) are used to develop the joint models (templates) for different lithologies. The P-wave velocity, attenuation, and conductivity are evaluated in terms of clay content, porosity, microfractures, and fluid type. The 3D joint AE rock physics templates (RPTs) are constructed based on the elastic attributes and conductivity, which are calibrated using the samples and log data. The templates are then applied to the shale-oil formations for rock property predictions.

Characteristics of shale-oil formations

Geological characteristics of the work area

The Ordos Basin, one of the most key regions with abundant hydrocarbon resources in China, consists of six tectonic elements, including the Yimeng uplift,

Western thrust belt, Tianhuan depression, Yishan slope, Weibei uplift, and Jinxi fold belt. In the Late Triassic, the basin was gradually closed and transformed from shallow sea deposits into lacustrine deposits (Ji et al., 2021). The tectonic activity and warm and humid climate led to a rapid expansion of the lake basin and the deposition of high-quality source rocks. The Chang 7 sedimentary period of the Yanchang Formations was the largest lacustrine period with high abundance, excellent type, and suitable maturity of organic matter, which is considered the most significant unconventional resource (shale-oil) in this basin (Shi et al., 2022). The largest shale-oil field in China was discovered in this basin in 2019, with geological reserves estimated to be over 1 billion tons, marking a significant breakthrough in shale-oil exploration in Chang 7 formations. The Chang 7 member mainly comprises muddy shale deposits interspersed with multiple thin layers of stacked sandstone. The effects of pore distribution, fluid properties, and rock wettability lead to a variation in the reservoir hydrocarbon expulsion efficiency for different lithologies. Sandstone has better expulsion efficiency and is the major target of this study, while the low efficiency and the mutual dissolution of hydrocarbons and organic matter in the shale lead to poor mobility and difficult development of hydrocarbons (Liu et al., 2021).

Core samples and log data

Seven sandstone samples (A–G) are collected from the target formations to evaluate the petrophysical characteristics of the shale-oil reservoirs. The muddy shale section is not sampled since it is not the major target, and sampling from that section is difficult. The rock samples are prepared in the shape of cylinders with diameters between 25.08 and 25.13 mm and lengths between 49.09 and 49.77 mm. The CTS and XRD experiments are conducted to analyze the mineralogy and pore structure of the samples. Table 1 shows the mineral components of the samples, namely, quartz, feldspar, clay, dolomite, calcite, and iron ore. The feldspar is mainly plagioclase and potassium feldspar, the plagioclase content is high, and the iron ore is mainly siderite. The CTSs of samples A and F at different scales are shown in Figure 1. The pore space is mainly composed of intergranular and dissolved pores and microfractures.

Table 1 Mineral components of rock samples

Samples	A	B	C	D	E	F	G
Quartz (%)	53.51	52.35	55.4	54.73	54.88	50.95	47.73
Feldspar (%)	28.49	31.55	26.07	24.92	31.61	26.67	24.31
Dolomite (%)	8.9	5.8	8.9	7.67	5.13	7.05	9.37
Calcite (%)	0.56	4.17	2.06	4.77	1.96	1.96	1.96
Clay (%)	6.03	5.59	5.85	7.16	5.35	10.96	15.23
Iron ore (%)	2.51	0.54	1.72	0.75	1.07	2.41	1.4

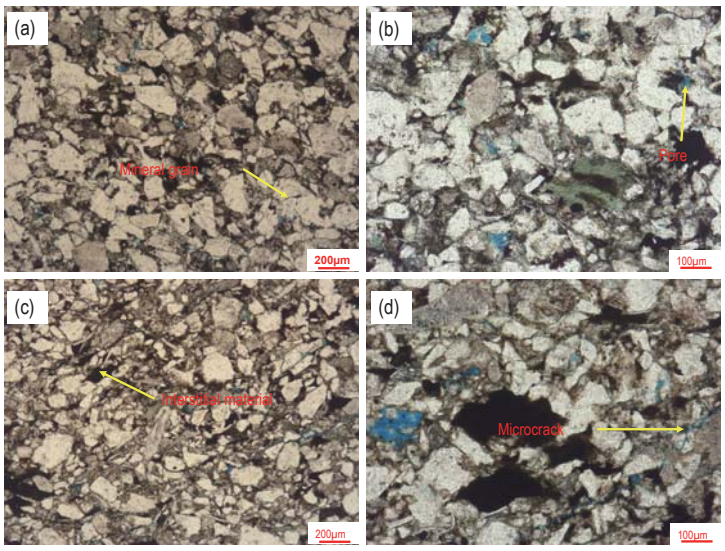

Figure 1. Cast thin sections of sandstone samples A (a, b) and F (c, d) at different scales.

The data on rock characteristics of the target layer, such as porosity (ϕ), P- and S-wave velocities (i.e. V_P and V_S), Poisson's ratio (ν), natural gamma (GR), and conductivity (σ) extracted from wells A and B are shown in Figures

2 and 3, where the red dashed box indicates sandstone section, and the porosity of muddy shale section could not be measured. Significant variations in the rock properties are observed, with low porosities and high natural gamma values. The reservoir is predominantly interbedded sandstone and shale layers, and large differences in the petrophysical characteristics between the two lithologies can be observed.

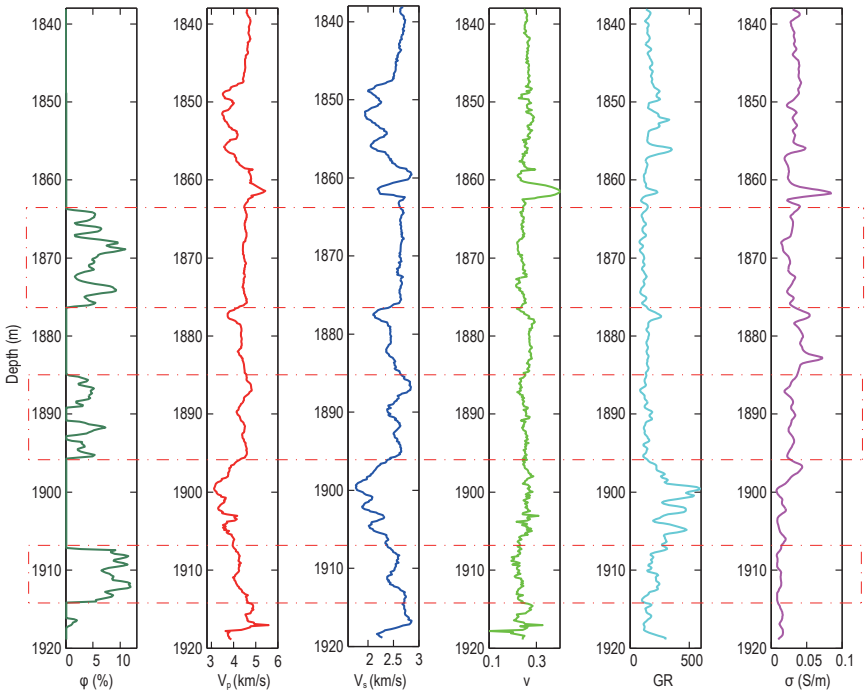

Figure 2. Target layer data of the shale-oil formations from well A. The columns from left to right represent porosity, P-wave velocity, S-wave velocity, Poisson's ratio, natural gamma, and electrical conductivity.

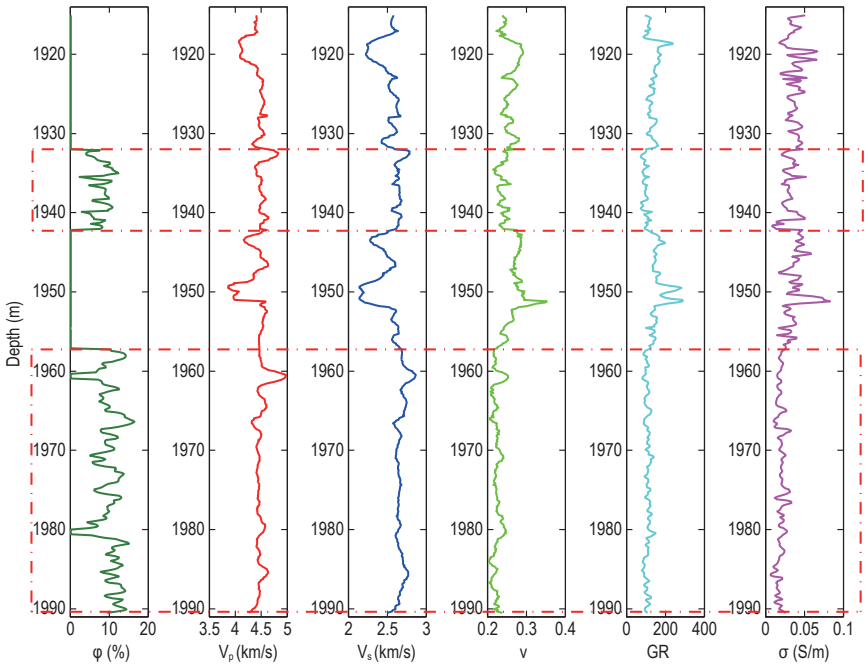

Figure 3. Target layer data of the shale-oil formations from well B. The columns from left to right represent porosity, P-wave velocity, S-wave velocity, Poisson's ratio, natural gamma, and electrical conductivity.

Acoustic-electrical properties of rock samples

The ultrasonic and electrical experiments are performed to analyze the effects of porosity, mineralogy, pressure (microfractures), and fluid saturation on the AE properties of the specimens under the different confining pressures and fluid saturation degrees (oil–water). The properties of the samples are given in Table 2.

Acoustic and electrical experiments

The ultrasonic pulse method is used to measure the wave velocities at a frequency of 0.55 MHz, temperature of 25°C, and pore pressure of 15 MPa. First, the varying pressure test is conducted as follows: the samples are dried in an oven and then saturated with water. They are sealed with a high-temperature-resistant rubber sleeve and finally placed in the experimental setup (Guo et al., 2009), which can withstand the high pressure, preventing the sample from being affected by the fluid used to exert the pressure. The samples are subjected to different confining pressures of 20, 30, 40, 50, and 60 MPa, and the waveforms transmitted through the rocks are

recorded. Samples B and D are selected for performing the tests at the different saturation levels (oil–water). The specimens are first saturated with oil, and then water is gradually injected under pressure. Approximately 20%, 40%, 60%, 80%, and 100% of pore water estimated from the volume are injected into the samples, and the waveforms are recorded.

Table 2 Physical properties of samples

Samples	A	B	C	D	E	F	G
Depth (m)	2036.5	1996.8	2341.5	1800	1996	1948.2	2000.6
Porosity (%)	3.56	4.631	7.33	8.853	10.16	5.28	4.49
Permeability (mD)	0.005	0.051	0.019	0.177	0.096	0.005	0.033
Clay content (%)	6.03	5.59	5.85	7.16	5.35	10.96	15.23
Density (g/cm^3)	2.58	2.44	2.48	2.37	2.37	2.53	2.57

The electrical test is performed to measure the conductivity of samples using the two-electrode method, resistivity experimental apparatus (Pang et al., 2022), and alternating current at a voltage of 1 V and a frequency of 120 Hz. The temperature and pressure maintained are the same as in the acoustic experiments. The rocks are saturated with brine (salinity of 56.5 g/L), placed in the device, and subjected to different pressures for measuring the conductivity. Similarly, samples B and D are used for performing the varying saturation experiments to measure the electrical resistances of samples, and the confining and pore pressures are set to 30 and 15 MPa, respectively. The conductivity σ (i.e., the reciprocal of the resistivity R_t) is calculated by

$$R_t = \frac{RS}{L}, \tag{1a}$$

$$\sigma = \frac{1}{R_t}, \tag{1b}$$

where L is the length of the sample, R is the resistance, and S is the cross-sectional area.

Acoustic and electrical properties

Figure 4 shows the variations of the elastic velocities and conductivity of the samples with respect to effective pressure, which is the difference between the confining and pore pressures. The velocities increase with the increasing pressure. With the increasing pressure, the rock microfractures gradually close, leading to an increase in the bulk and shear moduli as well as in the velocities. In addition, the electrical conductivity is shown to decrease with increasing pressure (microfracture content decreases). Figure 5 shows the variations in the AE properties versus water saturation for samples B and D. Smaller variations in the velocities with respect to fluid (oil–water) saturation are observed. The P-wave velocity increases and then decreases with water saturation, and the change is minimal. The S-wave velocity has a poor relationship with the saturation and no apparent trend. The experimental results show that there is a weak correlation between the velocities and saturation (Figures 5a–d). As shown in Figure 5e, the conductivity increases with water saturation and exhibits a stronger correlation.

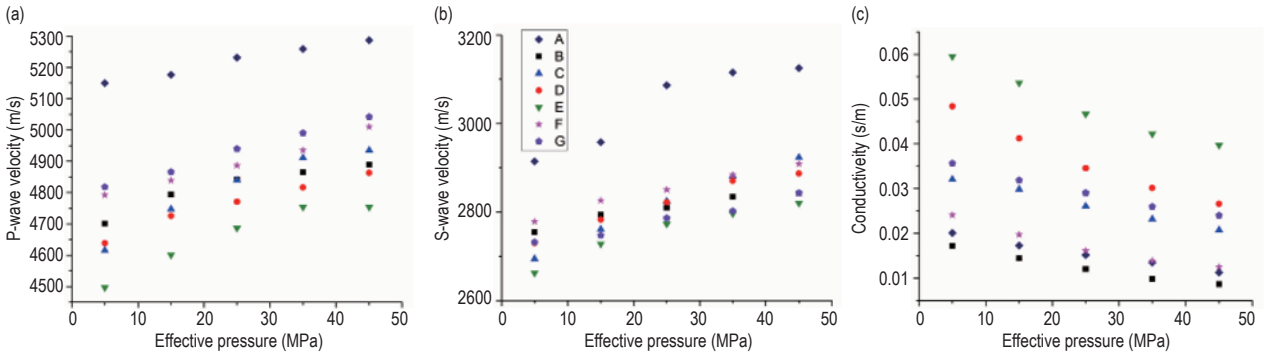

Figure 4. P-wave velocity (a), S-wave velocity (b), and conductivity (c) of rock samples (full water saturation) as a function of effective pressure.

The experimental data at the in-situ conditions (i.e., pore pressure and effective pressure of 15 MPa) are selected. The 3D diagrams of the variations in AE properties with respect to clay content (V_{sh}) and porosity of the samples are shown in Figure 6. In this study, samples A–E are predominantly clean sandstone (V_{sh} < 10%), and samples F and G are muddy sandstones (V_{sh} > 10%). Different sample types are given by different symbols in Figure 6, with black and red colors indicating clean and muddy sandstones, respectively. The AE properties of clean sandstones (samples A–E) are strongly related to porosity. The velocity and Poisson's ratio decrease with porosity while the conductivity increase. In addition, there is a minimal effect of clay content on the AE properties. The results indicate that the AE properties are mainly controlled by the pore-microfracture structure. In the case of the muddy sandstones (samples F and G), there is a decrease in the velocities and an increase in the Poisson ratio and conductivity with the increase of clay content (compared with sample A). The clay content is one of the most important factors affecting rock properties.

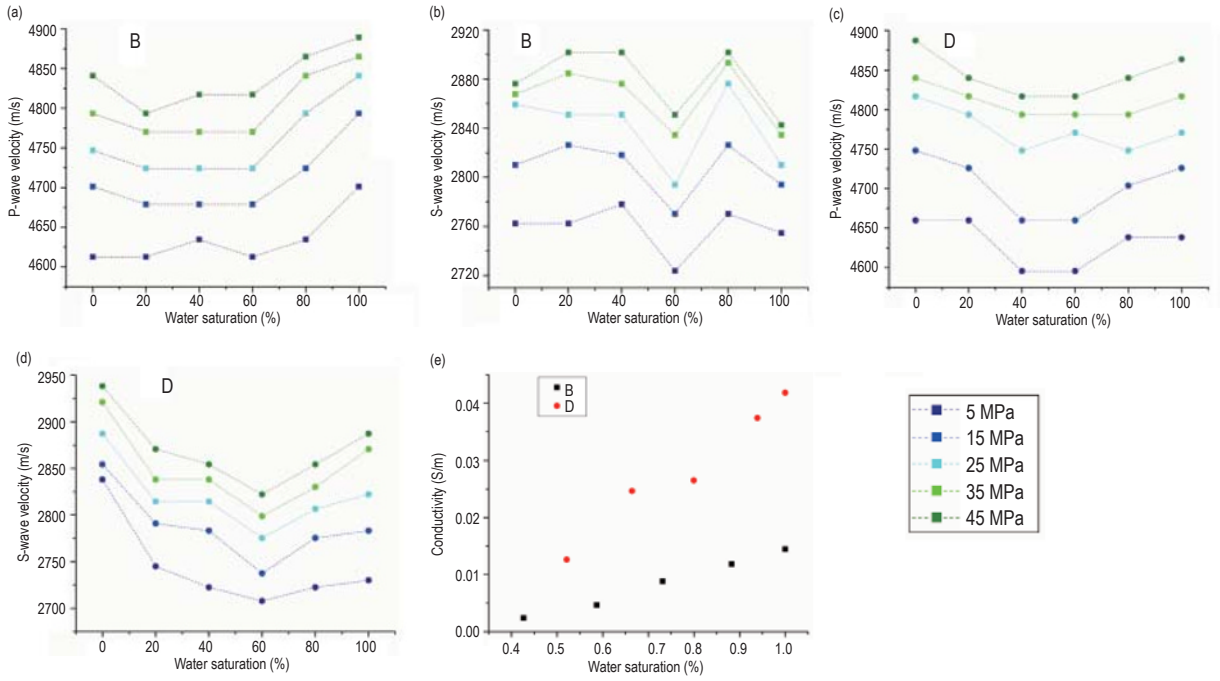

Figure 5. P-wave and S-wave velocities (a and b) of sample B as a function of water saturation; P-wave and S-wave velocities (c and d) of sample D as a function of water saturation; and conductivity (e) of samples B and D as a function of water saturation.

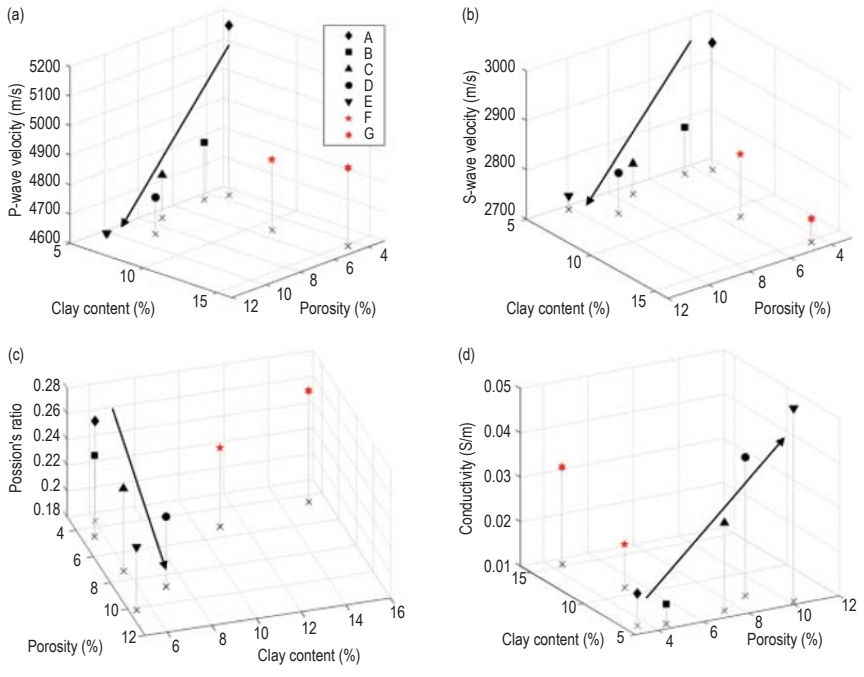

Figure 6. Variations in P-wave and S-wave velocities (a and b), Poisson's ratio (c), and conductivity (d) with respect to clay content and porosity in rocks.

The experimental data demonstrates that the microfractures (pressure) significantly affect the AE properties of the rocks,

indicating a strong correlation. The effect of saturation (oil–water) on the elastic properties is minimal, while the electrical response is dependent on the saturation and exhibits a monotonic trend. An increase in the porosity and clay content may lead to a decrease in the velocity and an increase in the conductivity. The Poisson ratio increases with clay content and decreases with porosity. The petrophysical properties of the clean and muddy sandstones are significantly different, and the major factors affecting them are also found to be different. The microfractures significantly affect the clean sandstone responses, while the influence of clay is negligible. On the other hand, the rock properties of muddy sandstones apparently depend on the clay content. Thus, the target formation sandstone is classified into clean and muddy sandstone sections for performing modeling analysis and reservoir identifications with the different lithologies.

Acoustic and electrical rock physics models

The target reservoirs are mainly composed of interbedded sandstone and muddy shale. In this work, the cores of the sandstone section of the reservoir are extracted to perform the ultrasonic and electrical experiments. The results show that the petrophysical characteristics of the core samples with clay content lower than 10% and those with clay content higher than 10% are significantly different; thus, the sandstone section is considered to be divided into clean sandstone (V_{sh} < 10%) and muddy sandstone (V_{sh} > 10%). In addition, the sandstone and shale sections can be identified based on the geological investigation and measured log data, and the AE rock physics models are applied to the three lithologies. The CTS and analysis of samples indicate that the clay minerals are mainly distributed around the rock grains in the sandstone and are the major supporting minerals forming the shale matrix and skeleton (Shi et al., 2021). Figure 7 shows the flow charts for the joint AE modeling.

Acoustic models

First, the acoustic models of (clean and muddy) sandstone and shale are proposed. The sandstone minerals are quartz, feldspar, clay, carbonate, and iron ore, while the shale minerals are mainly clay, quartz, feldspar, and carbonate. The elastic moduli of mineral mixture for the different lithologies are calculated using the HS equation by Berryman (1995) for a multiphase system (more than two),

$$K^{HS+} = \mathrm{M}(\mu_{max}) \qquad K^{HS-} = \mathrm{M}(\mu_{min})$$
$$\mu^{HS+} = \Gamma(\zeta(K_{max}, \mu_{max})) \qquad \mu^{HS-} = \Gamma(\zeta(K_{min}, \mu_{min})), \quad (2a)$$

$$\Lambda(z) = \left(\sum_{i=1}^{N} \frac{f_i}{K_i + \frac{4}{3}z} \right)^{-1} - \frac{4}{3}z, \quad (2b)$$

$$\Gamma(z) = \left(\sum_{i=1}^{N} \frac{f_i}{\mu_i + z} \right)^{-1} - z, \quad (2c)$$

$$\zeta(K, \mu) = \frac{\mu}{6}\left(\frac{9K + 8\mu}{K + 2\mu} \right), \quad (2d)$$

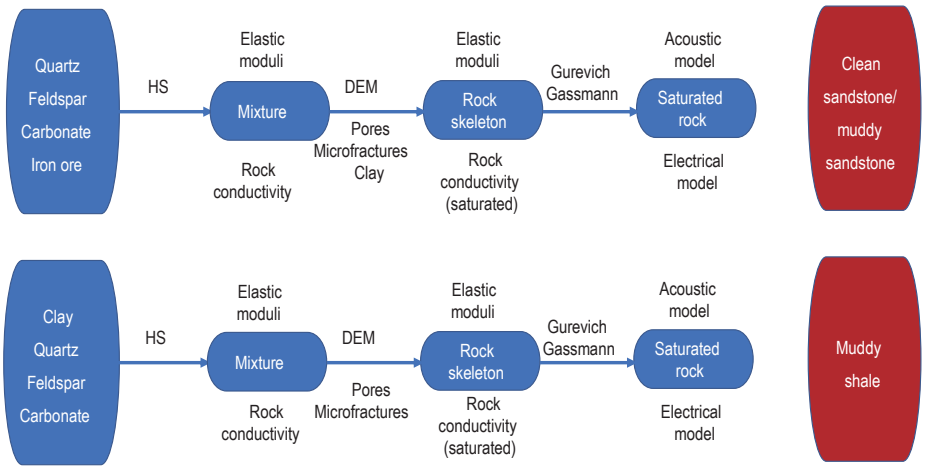

Figure 7. Joint acoustic-electrical modeling for different lithologies of shale-oil formation.

where K_i and μ_i are the elastic moduli of the ith component, respectively, and f_i is the corresponding volume fraction.

The pore, microfracture, or clay is added to the mineral mixture as an inclusion using DEM to obtain the elastic properties of dry rock. The microfractures in rocks tend to close with increasing pressure, and the higher the microfracture porosity, the lower the pressure (David and Zimmerman, 2012; Zhang et al., 2019), and the microfracture content can be used to match the experimental data at different pressures. According to Berryman (1992),

$$(1-y)\frac{\mathrm{d}}{\mathrm{dy}}[K^*(y)] = (K_2 - K^*)P^{(*2)}(y), \quad (3a)$$

$$(1-y)\frac{\mathrm{d}}{\mathrm{dy}}[\mu^*(y)] = (\mu_2 - \mu^*)Q^{(*2)}(y), \quad (3b)$$

with the initial conditions $K^*(0) = K_1$ and $\mu^*(0) = \mu_1$, where K_1 and μ_1 are the elastic moduli of the host, respectively, y represents the content of phase 2, K2 and μ2 are the corresponding moduli, and P^{*i} and Q^{*i} represent the geometric factors (Appendix A).

The fluid properties are obtained at in-situ conditions (Batzle and Wang, 1992), and the effective modulus of the mixed fluid is calculated (Wollner and Dvorkin, 2018; Monachesi et al., 2020, see Appendix A). The equations by Gurevich (2010) and Gassmann (1951) are used for estimating the wave responses of rocks containing fluids and complex pore structures. Gurevich et al. (2010) proposed a squirt flow model that simulates the squirt flow effects at different saturations, where compliant (soft) pores connected to stiff pores act as the fluid channels. The dry rock bulk and shear moduli (K_{bf} and μ_{bf}, respectively), including squirt flow effects, are calculated by

$$\frac{1}{K_{bf}} = \frac{1}{K_h} + \left(\frac{1}{\frac{1}{K_{dry}} - \frac{1}{K_h}} + \frac{3\omega i\eta}{8\phi_C \alpha_C} \right)^{-1}, \quad (4a)$$

$$\frac{1}{\mu_{bf}} = \frac{1}{\mu_{dry}} - \frac{4}{15}\left(\frac{1}{K_{dry}} - \frac{1}{K_{bf}} \right), \quad (4b)$$

where η is the fluid viscosity, ω is the angular frequency, and α_c is the microfracture aspect ratio. K_h is the bulk modulus of the frame containing only hard pores, and K_{dry} and μ_{dry} represent the bulk and shear moduli obtained with the DEM equations, respectively.

The P-wave and S-wave velocities and quality factors of a saturated rock are obtained based on the bulk and shear moduli as

$$V_S = \sqrt{\frac{\mu_{bf}}{\rho_{sat}}}, \quad (5a)$$

$$V_P = \sqrt{\left(\frac{4}{3}V_S^2 + \frac{K_{sat}}{\rho_{sat}} \right)}, \quad (5a)$$

$$Q_P = \frac{\mathrm{Re}(K_{sat} + 4\mu_{bf}/3)}{\mathrm{Im}(K_{sat} + 4\mu_{bf}/3)}, \quad (5c)$$

Table 3 Properties of acoustic models

Sandstone/ Muddy sandstone		Shale	
Grain bulk modulus (K_S)	45 GPa	Clay bulk modulus (K_{sh})	21 GPa
Grain shear modulus (μ_S)	40 GPa	Clay shear modulus (μ_{sh})	7 GPa
Grain density (ρ_S)	2.65 g/cm^3	Clay density (ρ_{sh})	2.55 g/cm^3
Clay bulk modulus (K_{sh})	21 GPa	Water bulk modulus (K_W)	2.24 GPa
Clay shear modulus (μ_{sh})	7 GPa	Water density (ρ_W)	1.002 g/cm^3
Clay density (ρ_{sh})	2.55 g/cm^3	Water viscosity (η_W)	0.98 × 10^{-3}
Water bulk modulus (K_W)	2.24 GPa	Oil bulk modulus (K_O)	1.27 GPa
Water density (ρ_W)	1.002 g/cm^3	Oil density (ρ_O)	0.79 g/cm^3
Water viscosity (η_W)	0.98 × 10^{-3}	Oil viscosity (η_O)	2.1 × 10^{-3}
Oil bulk modulus (K_O)	1.27 GPa	Pore Aspect Ratio	0.2
Oil density (ρ_O)	0.79 g/cm^3	Microfracture aspect ratio	0.001
Oil viscosity (η_O)	2.1 × 10^{-3}		
Pore Aspect Ratio	0.2		
Microfracture aspect ratio	0.001		

where ρ_{sat} is the density of saturated rock, and K_{sat} and μ_{sat} are the corresponding elastic moduli.

The shale-oil formations are divided into clean and muddy sandstones and shale. Based on the acoustic

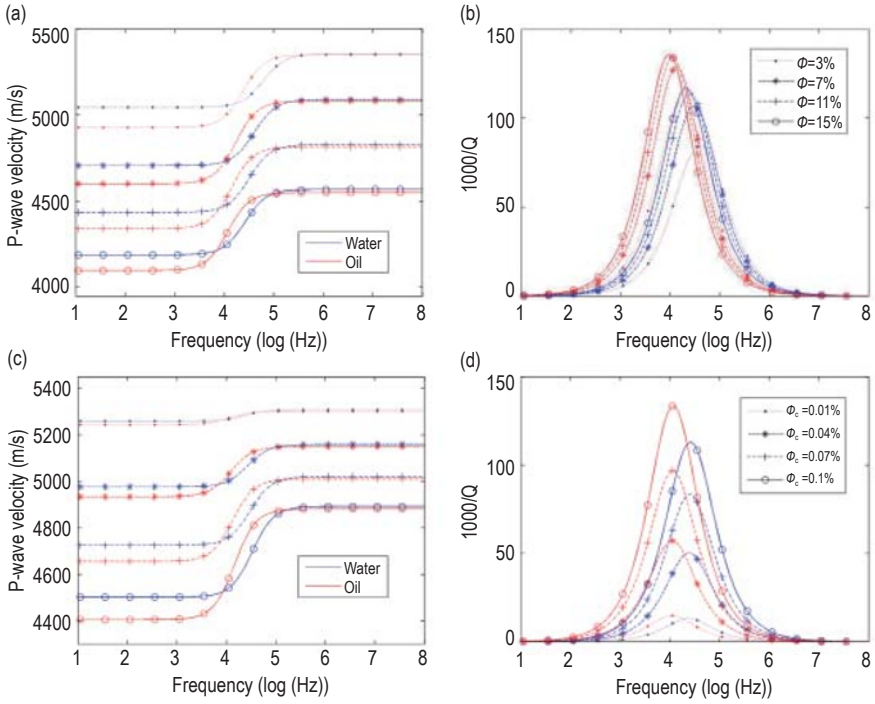

Figure 8. P-wave velocity (a) and attenuation (b) of clean sandstone versus frequency for different fluids and porosities (ΦC = 0.1%). P-wave velocity (c) and attenuation (d) versus frequency for different fluids and microfracture porosities (Φ = 10%). The clay content of the rocks is 5%.

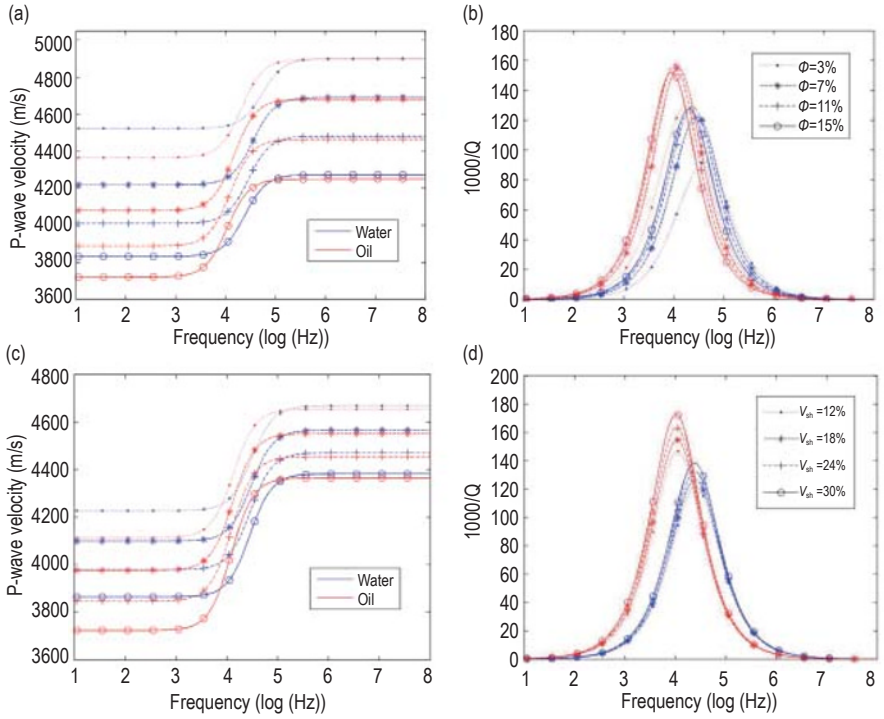

Figure 9. P-wave velocity (a) and attenuation (b) of muddy sandstone versus frequency for different fluids and porosities (V_{sh} = 10%). P-wave velocity (c) and attenuation (d) of muddy sandstone versus frequency for different fluids and clay contents (Φ = 10%). The microfracture porosity of the rocks is 0.1%.

models of different lithologies, the acoustic wave responses to total and microfracture porosities and fluid are analyzed in clean sandstone, and the responses to porosity, clay content, and fluid are analyzed in muddy sandstone and shale. The model properties are given in Table 3. The models are used to estimate the P-wave velocity and attenuation of clean sandstones (Figure 8), muddy sandstones (Figure 9), and shale (Figure 10) at various acoustic wave frequencies for different fluids with different total and microfracture porosities/clay contents. An increase in the porosity, microfracture porosity, and clay content leads to a decrease in P-wave velocity. The dispersion and attenuation increase with the two porosities, whereas the influence related to clay is weak. The model results demonstrate that the dispersion and attenuation for rocks saturated with oil are higher than those of rocks saturated with water, and the characteristic frequency of the former is at the lower frequency band compared with the latter.

Electrical models

The electrical models of sandstones and shale are proposed. The conductivity of the mineral mixture between the electrical HS boundaries is estimated. According to Berryman (1995), the equation for multiphase minerals (more than two) is given by

$$\sigma^{HS+} = \Gamma(\sigma_{max}) \quad \sigma^{HS-} = \Gamma(\sigma_{min}), \tag{6a}$$

$$\Gamma(q) = \left(\sum_{i=1}^{N} \frac{f_i}{\sigma_i + 2q} \right)^{-1} - 2q, \tag{6b}$$

where σ^{HS+} and σ^{HS-} represent the upper and lower boundaries, respectively. σ_{max} and σ_{min} are the maximum and minimum values, respectively, and σ_i is the conductivity of the ith component.

According to the microstructure properties of different lithologies, the conductivity of pores and microfractures containing fluids and clay are included in the electrical DEM model. The same factors (clay content, total and microfracture porosities, and aspect ratio) as the acoustic models are considered to calculate the conductivity. Similarly, considering the good correlation between pressure and microcracks, microfracture porosity is used to match the electrical data at different pressures. The effect of frequency on the conductivity is not considered, as the polarization effect on the conductivity is exceptionally low at the frequency considered in this study (Kirichek et al., 2019; Pang et al., 2022). In addition, since the salinity (56.5 g/L) in the target reservoirs is high (Leveaux and Poupon, 1971; Pang et al., 2022), the additional conductivity of clay is neglected, and only the contribution of the mineral to

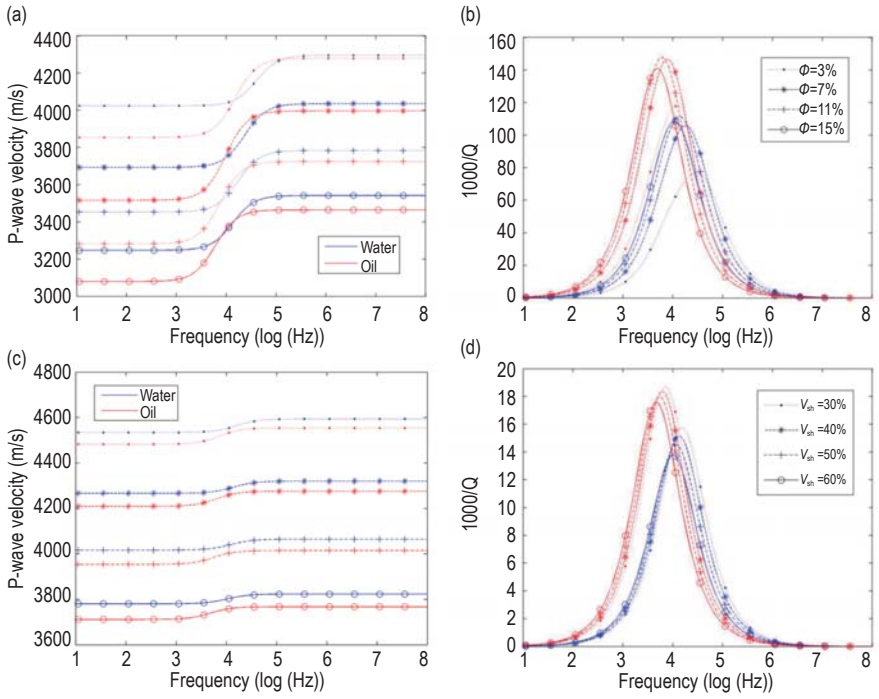

Figure 10. P-wave velocity (a) and attenuation (b) of shale versus frequency for different fluids and porosities (V_{sh} = 50%). P-wave velocity (c) and attenuation (d) of shale versus frequency for different fluids and clay content (Φ = 10%). The microfracture porosity of the rocks is 0.1%.

electrical properties is considered.

Cilli and Chapman (2021) described the electrical DEM as

$$(1-y)\frac{d}{dy}\left[\sigma^*(y)\right]=\left(\sigma_2-\sigma^*\right)\lambda, \quad (7)$$

where the initial condition is $\sigma^*(0) = \sigma_1$. σ_1 and σ_2 are the conductivities of the host and inclusion, respectively, and λ represents the coefficient related to the depolarization factor (Appendix B).

The electrical conductivity results of the three lithologies at varying clay content, total porosities, and microfracture porosities with different water saturation degrees are simulated based on the constructed model. For the properties of the model, the conductivities of mineral, brine, and clay are 0.01, 8.7, and 0.5 S/m, respectively, lithology coefficient and saturation index are 1 and 2, respectively, and pore structure (pore, microfracture, and clay inclusion aspect ratio) is the same as the acoustic model. Figure 11 shows the variations in conductivity with respect to total and microfracture porosities, clay content, and water saturation for the three lithologies. The conductivity increases with an increase in these properties, indicating a monotonic trend.

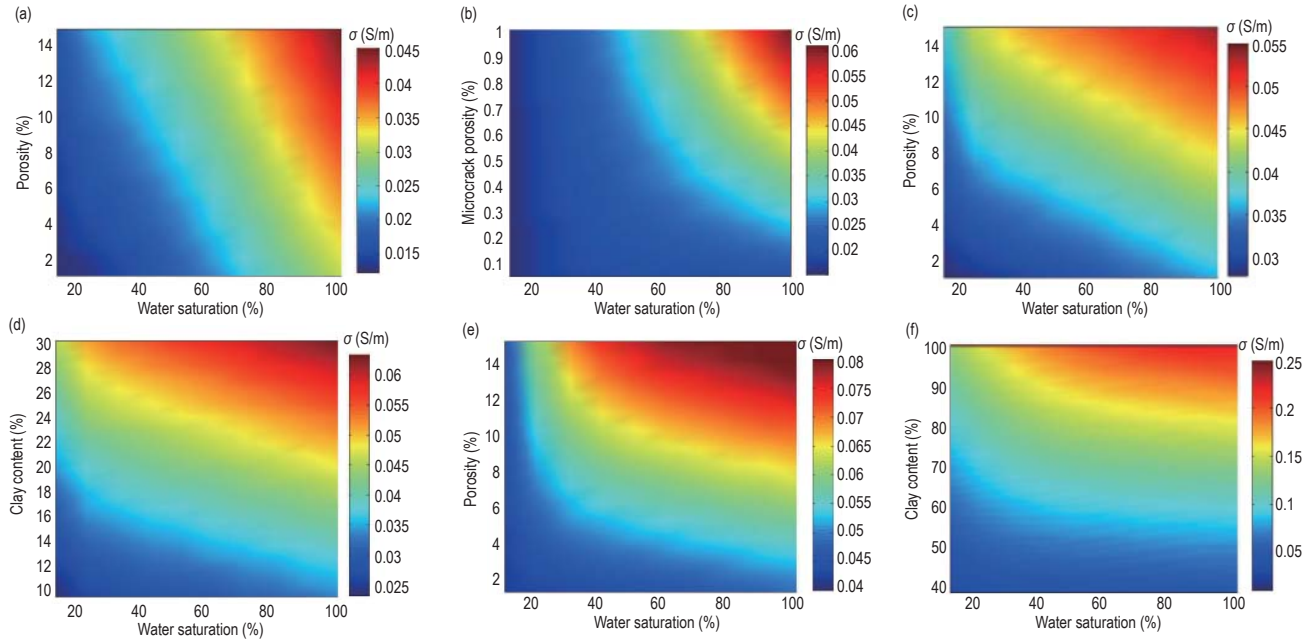

Figure 11. Conductivity of clean sandstone versus porosity (a), microfracture porosity (b), and water saturation; conductivity of muddy sandstone versus porosity (c), clay content (d), and water saturation; and conductivity of shale versus porosity (e), clay content (f), and water saturation.

Joint AE templates of shale-oil formations and their applications

Establishment and calibration of joint AE templates

The joint AE templates of shale-oil reservoirs are obtained based on the elastic and electrical attributes (conductivity, impedance of P wave (IP), and Poisson's ratio) in the forward modeling. The microfractures in rocks tend to close with increasing pressure, and higher microfracture porosity is associated with lower pressure (David and Zimmerman, 2012; Zhang et al., 2019). Thus, the samples at different effective pressures are considered to analyze the effect of microfractures on acoustic and electrical properties. The microfractures in sandstone significantly affect the AE properties, while the rock physical properties of muddy sandstone are dependent on clay content. Thus, the 3D AE templates of clean sandstone (regarding total and microfracture porosities and saturation) and muddy sandstone (regarding porosity, clay content, and saturation) are developed, as shown in Figures 12 and 13, respectively. The frequency is set to 0.55 MHz, and the color bar indicates the effective pressure. The ranges of model properties are set as follows: 3%–15% for porosity, 0.01%–0.5% for microfracture porosity, 10%–30% for

clay content, and 0%–100% for water saturation. The experimental data in Figure 12 show that a decrease in the pressure or an increase in the microfracture porosity leads to an increase in conductivity and Poisson's ratio and a decrease in the impedance, which is consistent with the template. Figure 13 shows that the porosity experimental data are in agreement with the template, and all the data points are distributed around the grid points of full water saturation. As the small variations of AE properties with respect to the pressure are observed, it can be inferred that the effect of microfractures on muddy sandstone is weak.

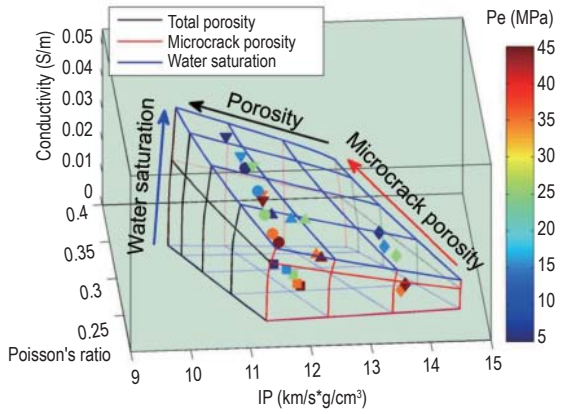

Figure 12. Joint acoustic-electrical template of clean sandstone compared with the experimental data. The scatters represent the samples (A–E), and the color bar is the effective pressure.

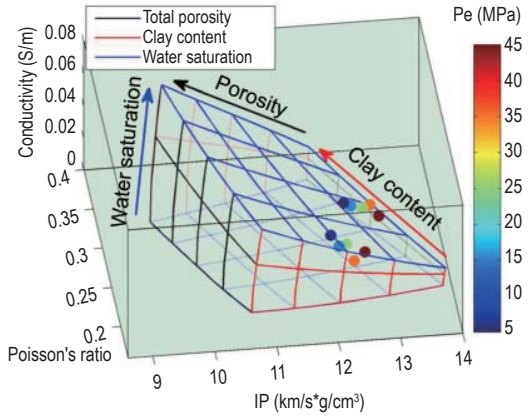

Figure 13. Joint acoustic-electrical template of muddy sandstone compared with the experimental data. The scatters represent the samples (F and G), and the color bar is the effective pressure.

The well-log data are extracted to calibrate the joint templates of the three lithologies. The target reservoirs consist of shale and sandstone, which can be distinguished based on the geological investigation and measured log data. Furthermore, the natural gamma values are used to estimate the clay content of formations (Appendix C), and the sandstone section is divided into clean sandstones (V_{sh} < 10%) and muddy sandstones (V_{sh} > 10%). Figure 14 shows the joint templates of the three lithologies and well-log data. To match the data

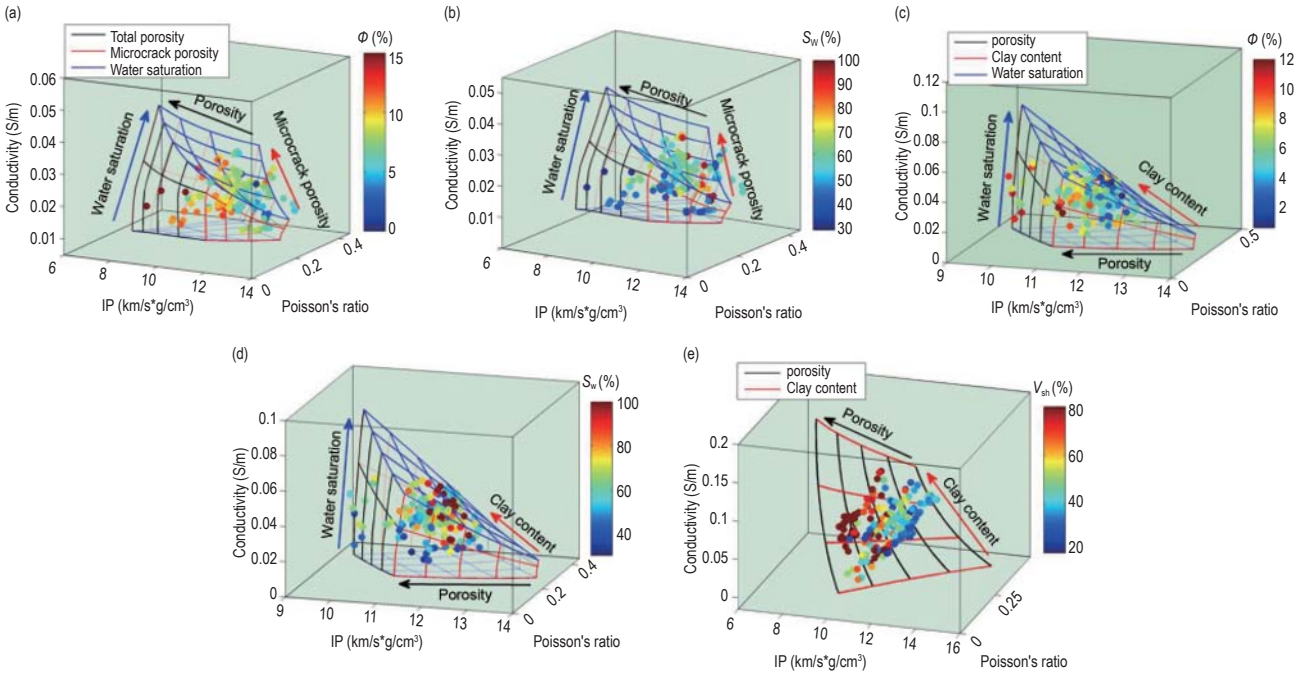

Figure 14. Joint acoustic-electrical templates of the shale-oil formations compared with well-log data. Clean sandstone with the color bar of porosity (a) and water saturation (b), muddy sandstone with the color bar of porosity (c) and water saturation (d), and shale with the color bar of clay content (e).

with the model, the frequency is set to 10 kHz, and the ranges of properties are considered, as shown in Table 4. The log interpretation indicates that the water saturation of the shale section is 100%, which is not considered in the template. The measured data of porosity, water saturation, and clay content are consistent with the template for the corresponding wave responses and conductivity. The elastic and electrical attributes can be obtained from the log data that are compared with RPTs for characterizing reservoir properties.

Table 4 Ranges of properties for templates

Sandstone		Muddy sandstone		Shale	
Porosity	3% - 15%	Porosity	3% - 15%	Porosity	1% - 20%
Microfracture porosity	0.1% - 0.5%	Clay content	10% - 30%	Clay content	15%-70%
Water saturation	0–100%	Water saturation	0–100%		

Practical applications of the work area

Reservoir prediction is performed based on the constructed 3D joint template and measured log data. The AE data of target layers from wells A and B are extracted for quantitative characterization of the three lithologies. To estimate the reservoir properties at wells A and B, we superimpose the elastic and electrical attributes on the 3D template and use a grid searching method. The estimations are assigned to the data by minimizing the sum of squares of the differences between the well-log data and the results provided by the template for the three attributes. The total porosity, microfracture porosity/clay content, and fluid (oil–water) saturation are estimated and compared with those from the log data. Figures 15 and 16 show the comparison of theoretical estimates and log data of the three sections. The results indicate that the target layer is tight, and the total and microfracture porosities are majorly distributed within the range of 0%–15% and 0%–0.5%, respectively, while larger variations of clay content and saturation are observed. The clay content of muddy sandstone and shale sections is high. In the case of sandstone sections, clean sandstone exhibits a higher porosity and lower water saturation compared with muddy sandstones. The porosity, clay content, and water saturation curves of the three lithological sections from log interpretations are shown to be basically consistent with the theoretical results by modeling. The predictions of porosity and clay content are in good agreement with the actual results, while some errors exist between the predicted results of the water saturation and the log interpretations. Experiments show that oil–water saturation is poorly

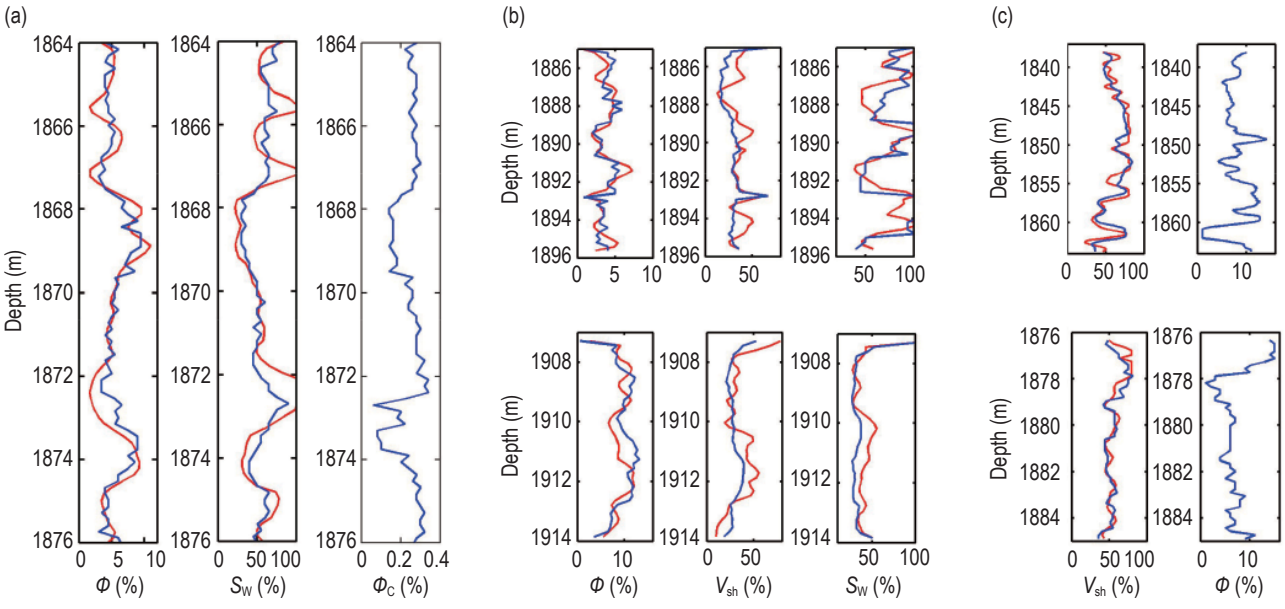

Figure 15. Theoretical and measured log curves of well A. (a) Sandstone, (b) muddy sandstone, and (c) shale. The red and blue lines represent measured and predicted data, respectively.

correlated with acoustic waves and highly dependent on electrical properties, making the prediction of saturation challenging.

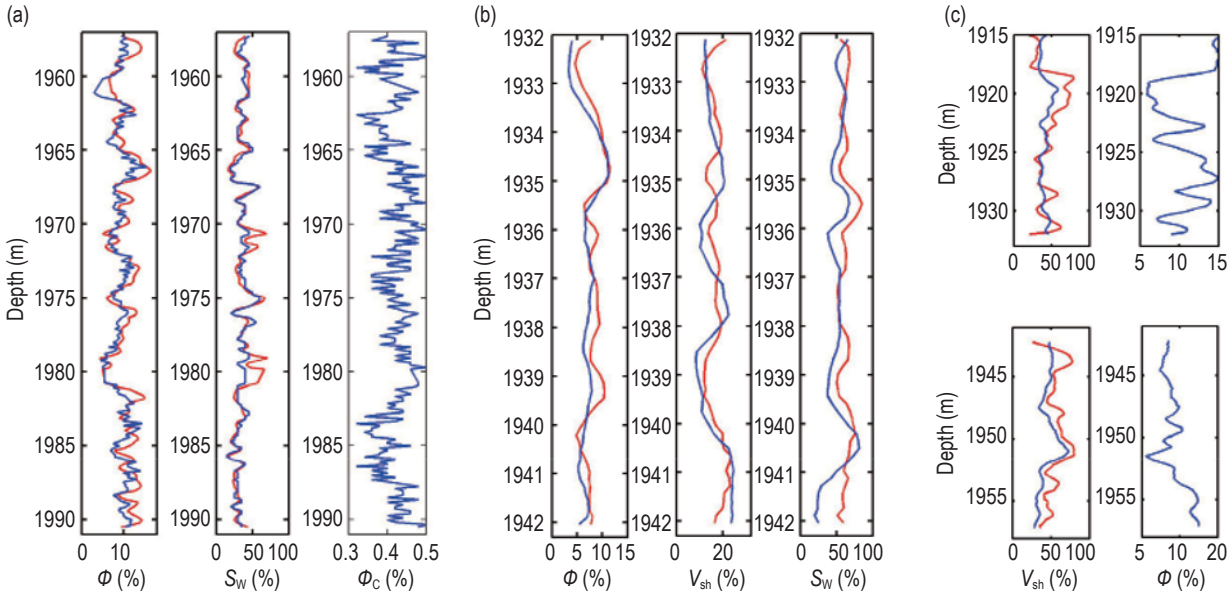

Figure 16. Theoretical and measured log curves of well B. (a) Sandstone, (b) muddy sandstone, and (c) shale. The red and blue lines represent measured and predicted data, respectively.

Conclusions

In this work, the lithology, pore structure, physical properties, and acoustic and electrical properties of the shale-oil formations are analyzed according to the XRD, CTS, ultrasonic wave, and conductivity tests. The joint AE models for different lithologies of the shale-oil formations are developed using the HS, DEM, Gurevich, and Gassmann equations, and the model estimates are compared and verified with the experimental and well-log data. Furthermore, the reservoir properties are estimated with the model and compared with those from the measured log data. The following conclusions are obtained.

(1) Shale oil formations in the work area have low porosity/permeability, complex characteristics of lithology, fluid distribution and pore structures, and strong heterogeneity. The reservoirs consist of interbedded sandstone and shale layers, and there are significant differences in the petrophysical properties between the sandstones and shales. Due to the different clay contents, the experimental results also indicate the apparent differences in AE properties between clean and muddy sandstones. The oil–water saturation has a weak effect on the elastic properties, while it strongly affects the conductivity.

(2) Different factors have an impact on how different lithologies respond to rocks. For clean sandstone, the microfractures significantly affect the AE properties, and the influence of clays is low. For muddy sandstone, the responses are dependent on the clay content. For shale rocks, clay minerals are the major supporting materials of the rock matrix and skeleton and play an important role in dominating the responses.

(3) Joint AE models for different lithologies in the shale-oil formations are built and applied to characterize the reservoir properties. The good agreement of theoretical modeling results and measured log data indicates that the joint model effectively characterizes and interprets the subsurface reservoirs, thereby providing a technical basis for the applications of AE data in the further geophysical exploration of complex tight formations.

Acknowledgments

We thank Dr. Han Xuehui of the China University of Petroleum (East China) for his assistance in the experimental tests. This work is supported by the National Natural Science Foundation of China (Nos. 41974123, 42174161), the Jiangsu Innovation and Entrepreneurship Plan and the Jiangsu Province Science Fund for Distinguished Young Scholars (grant no. BK20200021).

References

Aguilera, M. S., and Aguilera, R., 2003, Improved models for petrophysical analysis of dual porosity reservoirs: Petrophysics, **44**(01), 21–35.

Amalokwu, K., Best, I.A., Sothcott, J., et al., 2014, Water saturation effects on elastic wave attenuation in porous rocks with aligned fractures: Geophysical Journal International, **197**(2), 943–947.

Archie, G., 1942, The electrical resistivity log as an aid in determining some reservoir characteristics: Transactions of the AIME, **146**(1), 54–62, doi:10.2118/942054-G.

Asami, K., 2002, Characterization of heterogeneous systems by dielectric spectroscopy: Progress in Polymer Science, **27**(8), 1617–1659.

Ba, J., Xu, W., Fu, L., et al., 2017, Rock anelasticity due to patchy-saturation and fabric heterogeneity. A double-double porosity model of wave propagation: Journal of Geophysical Research: Solid Earth, **122**(3), 1949–1976, doi: 10.1002/2016JB013882.

Batzle, M., and Wang, Z., 1992, Seismic properties of pore fluids: Geophysics, **57**(11): 1396–1408.

Berryman, J. G., 1980, Long-wavelength propagation in composite elastic media: Journal of Acoustical Society of America, **68**(6), 1809–1831.

Berryman, J. G., 1992, Single-scattering approximations for coefficients in Biot's equations of poroelasticity: Acoustical Society of America Journal, **91**(2), 551–571.

Berryman, J. G., 1995, Mixture theories for rock properties. Rock physics phase relation: A Handbook Physics Constants, **3**, 205–228.

Chapman, S., Tisato, N., Quintal, B., et al., 2016, Seismic attenuation in partially saturated Berea sandstone submitted to a range of confining pressures: Journal of Geophysical Research: Solid Earth, **121**(3), 1664–1676.

Cilli, P., and Chapman, M., 2021, Linking elastic and electrical properties of rocks using cross-property DEM: Geophysical Journal International, **225**(3), 1812–1823.

David, E. C., and Zimmerman, R. W., 2012, Pore structure model for elastic wave velocities in fluid-saturated sandstones: Journal of Geophysical Research: Solid Earth, **117**(B7), B07210.

Dutilleul, J., Bourlange, S., Géraud, Y., et al., 2020, Porosity, pore structure, and fluid distribution in the sediments entering the northern Hikurangi margin, New Zealand: Journal of Geophysical Research: Solid Earth, **125**(11), e2020JB020330. https://doi.org/10.1029/2020JB020330.

Fan, J., F., Shi, J., Wan, X. et al., 2022, Classification evaluation method for Chang 7 oil group of Yanchang formation in Ordos Basin: Journal of Petroleum Exploration and Production Technology, **12**(11), 825–834. https://doi.org/10.1007/s13202-021-01338-4.

Feng, S., Niu, X., Liu, F., et al., 2013, Characteristics of Chang7 tight oil reservoir space in Ordos basin and its significance: Journal of Central South University, **44**(11), 4574–4580.

Gabàs, A., Macau, A., Benjumea, B., et al., 2016, Joint audio-magnetotelluric and passive seismic imaging of the Cerdanya Basin: Surveys in Geophysics, **37**(5), 897–921.

Gassmann, F., 1951, Elasticity of porous media: Vierteljahrsschrder Naturforschenden Gesselschaft, **96**, 1–23.

Gomez, C. T., Dvorkin, J., and Vanorio, T., 2010, Laboratory measurements of porosity, permeability, resistivity, and velocity on Fontainebleau sandstones: Geophysics, **75**(6), E191–E204.

Gurevich, B., Makarynska, D., de Paula, O. B., et al., 2010, A simple model for squirt-flow dispersion and attenuation in fluid-saturated granular rocks: Geophysics, **75**(6), N109–N120.

Guo, M. Q., Fu, L. Y., Ba, J., 2009, Comparison of stress-associated coda attenuation and intrinsic attenuation from ultrasonic measurements: Geophysical Journal International, **178**(1), 447–456.

Han, T., 2018, Joint elastic-electrical properties of artificial porous sandstone with aligned fractures: Geophysical Research Letters, **45**(7), 3051–3058.

Han, T., Best, A., Sothcott, J., et al. 2011. Joint elastic-electrical properties of reservoir sandstones and their relationships with petrophysical parameters: Geophysical Prospecting, **59**(3), 518–535.

Han, T., Wei, Z., and Li, F., 2020, How the effective pore and grain shapes are correlated in Berea sandstones: Implications for joint elastic-electrical modeling: Geophysics, **85**(3), MR147–MR154.

Iwamori, H., Ueki, K., Hoshide, T., et al., 2021, Simultaneous analysis of seismic velocity and electrical conductivity in the crust and the uppermost mantle: A forward model and inversion test based on grid search: Journal of Geophysical Research: Solid Earth, **126**(9), e2021JB022307.

Ji, X., Wang, H., Ge, Y., et al., 2022, Empirical mode decomposition-refined composite multiscale dispersion entropy analysis and its application to geophysical well log data: Journal of Petroleum Science and Engineering, **208**(12), 109495, https://doi.

org/10.1016/j.petrol.2021.109495.

Kazatchenko, E., Markov, M., and Mousatov, A., 2004, Joint modeling of acoustic velocities and electrical conductivity from unified microstructure of rocks: Journal of Geophysical Research, **109**(B1), B01202, doi:10.1029/2003JB002443.

Kirichek, A., Chassagne, C., and Ghose, R., 2019, Predicting the dielectric response of saturated sandstones using a 2-electrode measuring system: Frontiers in Physics, **6**(148), doi: 10.3389/fphy.2018.00148.

Leveaux, J., and Poupon, A., 1971, Evaluation of water saturation in shaly formations: The Log Analyst, **12**(4), SPWLA-1971-vXIIn4a1.

Li, M., Tang, Y., Bernabé, Y., et al., 2015, Pore connectivity, electrical conductivity, and partial water saturation: network simulations: Journal of Geophysical Research: Solid Earth, **120**(6), 4055–4068.

Li, X., Li, C., Li, B., et al., 2020, Response laws of rock electrical property and saturation evaluation method of tight sandstone: Petroleum Exploration and Development, **47**(1), 214–224.

Li, Z., 2018, Processing and comprehensive interpretation of geophysical well-logging data: Beijing Geological Publisher (in Chinese).

Liu, Q., Li, P., Jin, Z. et al., 2022, Organic-rich formation and hydrocarbon enrichment of lacustrine shale strata: A case study of Chang 7 Member: Science China Earth Sciences, **65**(1), 118–138.

Ma, R., and Ba, J., 2020, Coda and intrinsic attenuations from ultrasonic measurements in tight siltstones: Journal of Geophysical Research, **125**(4), e2019JB018825.

Mavko, G., Mukerji, T., and Dvorkin, J., 2009, The rock physics handbook: tools for seismic analysis of porous media: Cambridge University Press.

Monachesi, L., Wollner, U., and Dvorkin, J., 2020, Effective pore fluid bulk modulus at patchy saturation: An analytic study: Journal of Geophysical Research: Solid Earth, **125**(1), e2019JB018267, doi.org/10.1029/2019JB018267.

Osborn, J. A., 1945, Demagnetizing factors of the general ellipsoid: Physical review, 67(11–12), 351.

Pang, M., Ba, J., Carcione, J., et al., 2019, Estimation of porosity and fluid saturation in carbonates from rock-physics templates based on seismic Q: Geophysics, **84**(6), M25–M36.

Pang, M., Ba, J., and Carcione, J. M., 2021a, Seismic identification of tight-oil reservoirs by using 3D rock-physics templates: Journal of Petroleum Science and Engineering, **201**(8), 108476.

Pang, M., Ba, J., Carcione, J. M., et al., 2021b, Elastic-electrical rock-physics template for the characterization of tight-oil reservoir rocks: Lithosphere, Special **3**, 3341849.

Pang, M., Ba, J., Carcione, J. M. et al., 2022, Acoustic and electrical properties of tight rocks: A comparative study between experiment and theory: Surveys in Geophysics, **43**(3), 1761–1791, https://doi.org/10.1007/s10712-022-09730-3.

Pride, S. R., Berryman, J. G., Commer, M. et al., 2017, Changes in geophysical properties caused by fluid injection into porous rocks: Analytical models: Geophysical Prospecting, **65**(3), 766–790.

Shi, J., Zou, Y., Cai, Y., et al., 2021, Organic matter enrichment of the Chang 7 member in the Ordos Basin: Insights from chemometrics and element geochemistry: Marine and Petroleum Geology, **135**(3–4), 105404.

Solazzi, S.G., Guarracino, L., Rubino, J.G. et al., 2019, Saturation Hysteresis Effects on the Seismic Signatures of Partially Saturated Heterogeneous Porous Rocks: Journal of Geophysical Research: Solid Earth, **124**(11), 11316–11335.

Soleymanzadeh, A., Kord, S., and Monjezi, M., 2021, A new technique for determining water saturation based on conventional logs using dynamic electrical rock typing: Journal of Petroleum Science and Engineering, **196**(3–4), 107803.

Sun, H., Duan, L., Liu, L., et al., 2019, The influence of micro-fractures on the flow in tight oil reservoirs based on pore-network models: Energies, **12**(21), 4104.

Wang, Q., Tao, S., and Guan, P., 2020, Progress in research and exploration & development of shale oil in continental basins in China: Natural Gas Geoscience, **31**(3), 417–427.

Wang, S., Tan, M., Wang, X., et al., 2022, Microscopic response mechanism of electrical properties and saturation model establishment in fractured carbonate rocks: Journal of Petroleum Science and Engineering, **208**(1), 109429.

Wollner, U., and Dvorkin, J., 2018, Effective bulk modulus of the pore fluid at patchy saturation: Geophysical Prospecting, **66**(6), 1372–1383.

Yan, W., Sun, J., and Golsanami, N., et al., 2019, Evaluation of wettabilities and pores in tight oil reservoirs by a new experimental design: Fuel, **252**, 272–280.

Yan, W., Sun, J., Zhang, J., et al., 2018, Studies of electrical properties of low-resistivity sandstones based on digital rock technology: Journal of Geophysics and Engineering, **15**(1), 153–163.

Yang, H., Niu, X., Xu, L., et al., 2016, Exploration potential of shale oil in Chang7 Member, Upper Triassic Yanchang Formation, Ordos Basin, NW China: Petroleum Exploration and Development, **43**(4), 511–520.

Yang, Z., and Zou, C., 2019, Exploring petroleum inside source kitchen: connotation and prospects of source rock oil and gas: Petroleum Exploration and Development, **46**(1), 173–184.

Ziarani, A. S., and Aguilera, R., 2012, Pore-throat radius and tortuosity estimation from formation resistivity data for tight-gas sandstone reservoirs: Journal of Applied Geophysics, **83**, 65–73.

Zou, C., Zhang, G., Yang, Z., et al., 2013, Geological concepts, characteristics, resource potential and key techniques of unconventional hydrocarbon: on unconventional petroleum geology: Petroleum Exploration and Development, **40**(4), 385–399.

Zhang, L., Ba, J., Carcione, J. M., et al., 2019, Estimation of pore microstructure by using the static and dynamic moduli: International Journal of Rock Mechanics and Mining Sciences, **113**: 24–30.

Zhang, L., Ba, J., and Carcione, J. M., 2021, Wave propagation in infinituple-porosity media: Journal of Geophysical Research: Solid Earth, **126**(4): e2020JB021266.

Zhang, L., Ba, J., Carcione, J. M., et al., 2022, Seismic wave propagation in partially saturated rocks with a fractal distribution of fluid-patch size: Journal of Geophysical Research: Solid Earth, **127**(2), e2021JB023809.

Appendix A: Acoustic model

According to Berryman (1980) and Mavko et al. (2009), the coefficients P and Q are

$$P=\frac{1}{3}T_1, \quad Q=\frac{1}{5}\left(T_2-\frac{1}{3}T_1\right), \tag{A-1}$$

where

$$T_1=\frac{3F_1}{F_2} \quad T_2-\frac{1}{3}T_1=\frac{2}{F_3}+\frac{1}{F_4}+\frac{F_4F_5+F_6F_7-F_8F_9}{F_2F_4}, \tag{A-2}$$

with

$$F_1=1+G\left[\frac{3}{2}(g+\theta)-J\left(\frac{3}{2}g+\frac{5}{2}\theta-\frac{4}{3}\right)\right], \tag{A-3}$$

$$F_2=1+G\left[1+\frac{3}{2}(g+\theta)-\frac{J}{2}\left(\frac{3}{2}g+5\theta\right)\right]+H\left(3-4J\right)+\frac{G}{2}\left(G+3H\right)\left(3-4J\right)\left[g+\theta-J\left(g-\theta+2\theta^2\right)\right], \tag{A-4}$$

$$F_3=1+G\left[1-(g+\frac{3}{2}\theta)+J\left(g+\theta\right)\right], \tag{A-5}$$

$$F_4=1+\frac{G}{4}\left[g+3\theta-J\left(g-\theta\right)\right], \tag{A-6}$$

$$F_5=G\left[-g+J\left(g+\theta-\frac{4}{3}\right)+H\theta\left(3-4J\right)\right], \tag{A-7}$$

$$F_6=1+G\left[1+g-J\left(g+\theta\right)+H\left(1-\theta\right)\left(3-4J\right)\right], \tag{A-8}$$

$$F_7=2+\frac{G}{4}\left[3g+9\theta-J\left(3g+5\theta\right)\right]+H\theta\left(3-4J\right), \tag{A-9}$$

$$F_8=G\left[1-2J+\frac{g}{2}\left(J-1\right)+\frac{\theta}{2}\left(5J-3\right)\right]+H\left(1-\theta\right)\left(3-4J\right), \tag{A-10}$$

$$F_9=G\left[\left(J-1\right)g-J\theta\right]+H\theta\left(3-4J\right), \tag{A-11}$$

with

$$G=\mu_i/\mu_m-1, \tag{A-12}$$

$$H=\frac{1}{3}\left(K_i/K_m-\mu_i/\mu_m\right), \tag{A-13}$$

$$J=\left[\left(1-2v_m\right)/2\left(1-v_m\right)\right], \tag{A-14}$$

where K_m, μ_m, and v_m represent the bulk and shear moduli and Poisson's ratio of the host phase, respectively. K_i and μ_i represent the bulk and shear moduli of phase i, respectively, and

$$\theta=\left\{\begin{array}{l}\dfrac{\alpha}{\left(\alpha^2-1\right)^{3/2}}\left[\alpha\left(\alpha^2-1\right)^{1/2}-\cosh^{-1}\alpha\right]\\ \dfrac{\alpha}{\left(1-\alpha^2\right)^{3/2}}\left[\cos^{-1}\alpha-\alpha\left(1-\alpha^2\right)^{1/2}\right]\end{array}\right\}, \tag{A-15}$$

where α is the aspect ratio with $\alpha > 1$ for prolate and $\alpha < 1$ oblate spheroids, and

$$g = \frac{\alpha^2}{1-\alpha^2}\left(3\theta - 2\right). \tag{A-16}$$

An approximate method for computing the effective bulk modulus of a mixed fluid was proposed in previous studies (Wollner et al., 2018; Monachesi et al., 2020),

$$\overline{K}_f = 0.75K_{f,\mathrm{AR}} + 0.25K_{f,\mathrm{HR}}, \tag{A-17}$$

with

$$K_{f,\mathrm{AR}} = f_1K_{f,1} + f_2K_{f,2}, \tag{A-18}$$

$$K_{f,\mathrm{HR}} = \left(\frac{f_1}{K_{f,1}} + \frac{f_2}{K_{f,2}}\right)^{-1}, \tag{A-19}$$

where f_1 and f_2 are the water and oil saturations, respectively.

Appendix B: Electrical model

The coefficient λ in the electrical DEM is obtained (Osborn 1945; Asami 2002) as

$$\lambda = \frac{1}{3}\sum_{P=1}^{3}\left\{\left[1 + \left(\frac{\sigma_2}{\sigma^*} - 1\right)L_P\right]^{-1}\right\}, \tag{B-1}$$

where L_P is the depolarization factor of phase 2, which is considered an ellipsoid inclusion ($\alpha < 1$) in this study, and

$$L_3 = \frac{1}{1-\alpha^2} - \frac{\alpha}{(1-\alpha^2)^{3/2}}\cos^{-1}\alpha, \tag{B-2}$$

$$L_1 = L_2 = (1 - L_3)/2. \tag{B-3}$$

According to Archie's equation (1942), the conductivity of pores and microfractures is given by

$$\sigma_2 = \beta^{-1}S_{\mathrm{W}}^{n}\sigma_{\mathrm{W}}, \tag{B-4}$$

where σ_{w} represents the brine conductivity, S_{w} is the water saturation, and σ_2 represents the conductivity of pores or microfractures, which equals σ_{w} when the water saturation is 1 (Aguilera and Aguilera, 2003; Pang et al., 2021b), n refers to the saturation index, and β is the lithology coefficient.

Appendix C: Clay volume estimation

The clay content of the formations can be calculated using the gamma-ray log. The gamma values of the mudstone and clean sandstone are considered as the maximum and minimum values, respectively, which are used to compare with the results of the target rocks (Li, 2018),

$$I_{\mathrm{GR}} = \left(GR - GR_{\mathrm{min}}\right)/\left(GR_{\mathrm{max}} - GR_{\mathrm{min}}\right), \tag{C-1}$$

$$V_{\mathrm{sh}} = \left(2^{\mathrm{GCUR}*I_{\mathrm{GR}}} - 1\right)/\left(2^{\mathrm{GCUR}} - 1\right), \tag{C-2}$$

where GR, GR_{min}, and GR_{max} denote the natural gamma values of the reservoirs, sandstone, and mudstone, respectively. I_{GR} is the mud-content index, and $GCUR$ is the Hirsch index (2).

Pang Meng-Qiang received his B.S. in Geological Engineering from Tianjin Chengjian University in 2017. He is presently a Ph.D. student in the School of Earth Sciences and Engineering at Hohai University. His research interests are rock physics model, reservoir prediction and acoustic and electrical properties.